PHYSICAL REVIEW A VOLUME 50, NUMBER 1 JULY 1994

Measurements of cross sections for electron-impact excitation into the metastable levels of argon and number densities of metastable argon atoms

R. Scott Schappe, M. Bruce Schulman,* L. W. Anderson, and Chun C. Lin
Department of Physics, University of Wisconsin, Madison, Wisconsin 53706

(Received 20 December 1993)

The technique of laser-induced fluorescence (LIF) has been applied to measure the cross sections for electron-impact excitation into the metastable levels of argon atoms as well as the number densities of the argon metastable atoms produced by electron excitation. A monoenergetic electron beam excites the ground-state atoms into the $3p^5 4s\ ^3P_0, ^3P_2$ metastable levels ($1s_3$ and $1s_5$ in Paschen's notation) and a pulsed laser pumps the atoms of a metastable level to a level in the $3p^5 4p$ configuration ($2p$ in Paschen's notation). The transient LIF from the $2p$ level is shown to be proportional to the apparent cross section of the metastable level and to the metastable number densities so that measurements of LIF enable us to determine both metastable cross sections and number densities. Methods for absolute calibration are described. We obtain both the apparent and direct excitation cross sections for each of the two metastable levels for electron energies from threshold to 200 eV and the results are compared with previous experimental and theoretical works. The pulsed LIF technique is also used to determine the disappearance rates of the metastable atoms after the electron beam is turned off. Two distinct decay modes are found and the observed behaviors are consistent with calculations based on diffusion theory.

PACS number(s): 34.80.Dp

I. INTRODUCTION

The study of rare gases is essential in understanding the fundamental physics of electron excitation of atoms. In addition, electron-impact cross sections of rare gases are of great technological interest because of the critical role Ne, Ar, Kr, and Xe atoms play in a variety of commercial devices such as discharge light sources [1] and laser systems [2]. Good phenomenological modeling of these devices requires accurate knowledge of the absolute cross sections. Metastable atoms, in particular, figure prominently in these models because of their very long lifetimes (> 1 sec) [3,4] and relatively large cross sections.

A large number of cross sections in Ne and Ar have been previously measured. Sharpton *et al.* [5] measured the excitation function shapes and cross sections for some 50 levels of Ne. They also demonstrated that, although Ne does not conform to *LS* coupling, by expressing the wave function of the excited level in terms of *LS* eigenfunctions, they could characterize the various experimental cross-section shapes and magnitudes. Ballou, Lin, and Fajen [6] performed a similar study on over 30 levels of Ar and showed that the same theoretical framework could be extended to explain the experimental results.

These earlier studies of Ne and Ar used the optical method and were therefore limited to studying levels from which optical radiation can be observed. For this reason it is not possible to investigate the metastable levels by the optical method without modification. Neon has a ground-state configuration of $1s^2 2s^2 2p^6\ ^1S_0$ and argon's ground-state configuration is similar: $[\mathrm{Ne}]3s^2 3p^6\ ^1S_0$. The lowest excited configuration for either atom is $ns^2 np^5 (n+1)s$, which consists of four energy levels designated $1s_2$, $1s_3$, $1s_4$, and $1s_5$ in Paschen's notation with total angular momentum $J=1$, 0, 1, and 2, respectively. An energy-level diagram of the Ar atom is shown in Fig. 1. The $1s_3$ and $1s_5$ levels are very nearly pure $^3P_0$ and $^3P_2$ levels and are not optically connected to the ground level, making them metastable. One method

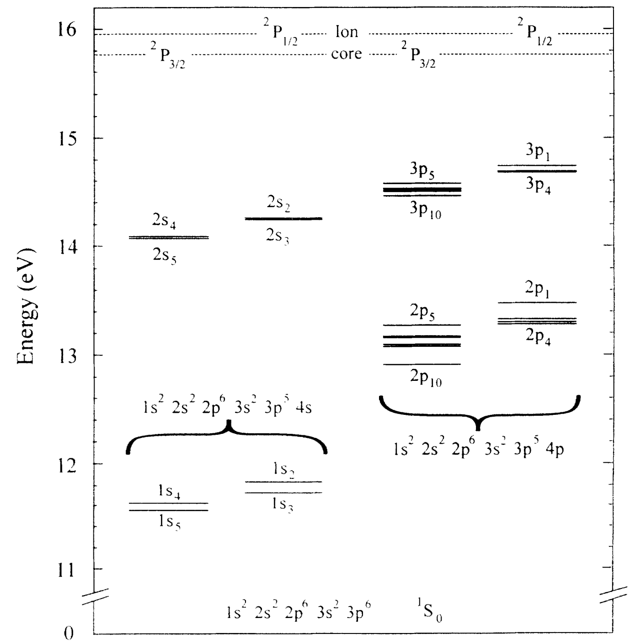

FIG. 1. Energy-level diagram of the argon atom. The Paschen notation ($1s_2$, $1s_3$, $1s_4$, and $1s_5$ and $2p_1, 2p_2, \ldots, 2p_{10}$) is used to label the energy levels associated with the $1s^2 2s^2 2p^6 3s^2 3p^5 4s$ and the $1s^2 2s^2 2p^6 3s^2 3p^5 4p$ configurations.

---

*Present address: Westinghouse Science and Technology Center, Pittsburgh, PA 15235.

1050-2947/94/50(1)/444(18)/$06.00

for measuring the cross sections for excitation into the metastable levels is the laser-induced fluorescence (LIF) technique, illustrated schematically in Fig. 2. The electron beam excites a ground level atom into level *a* (metastable). A dye laser is tuned to the transition between levels *a* and *b*. Atoms in level *a* are pumped by the laser into level *b*, from which they spontaneously decay into level *c*. As we show in Sec. II B, the intensity of the *b* to *c* radiation is directly proportional to the apparent cross section for excitation into the metastable level.

This method has been applied using a cw dye laser to measure the absolute electron-excitation cross sections into the $1s_3$ and $1s_5$ metastable levels of Ne [7]. The spectral range of a cw dye laser is generally limited at the low-wavelength end by the pump wavelength. Pulsed lasers, on the other hand, can produce very high energy densities so that the laser light can be frequency doubled and Raman shifted, thereby extending the range of tunable output wavelengths beyond the pump wavelength down into the vacuum ultraviolet [8]. This allows the study of a wider variety of atomic energy levels by the LIF method. Also, the lower power of the cw laser may not be sufficient to saturate completely the entire Doppler profile of a line: this makes it difficult to describe in absolute terms the pumping rate of all of the atoms in the Doppler distribution. Conversely, the high power and large bandwidth of the pulsed laser permits the saturation of the entire Doppler profile so that it is possible to know the pumping rates and consequently to measure the absolute metastable number densities. The short pulse duration also makes the pulsed laser suitable for time-resolved density measurements. In this paper we report the application of the LIF technique using a pulsed laser to measure absolutely the Ar metastable cross sections and number densities as well as the disappearance rates for the metastable atoms of Ar.

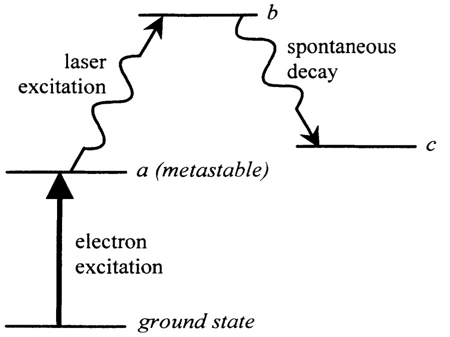

FIG. 2. Schematic diagram of the LIF process. A steady-state electron beam excites ground-state Ar atoms into the metastable level (*a*), then a short dye-laser pulse pumps the atoms into a higher level (*b*), which then spontaneously decays to a third level (*c*). The intensity of the transient $b \rightarrow c$ emission produced by the laser pumping of the metastable atoms is proportional to the apparent cross section for the electron excitation into the metastable level.

II. METHOD

A. Qualitative description

In the experiments of Ref. [7], an electron beam excites ground-state atoms to a 1*s* metastable level. A cw laser pumps the metastable atoms into a level in the $np^5(n+1)p$ configuration, called $2p_i$ in Paschen's notation (with $i=1,2,\ldots,10$). If the laser pumping rate for the $1s$-$2p_i$ transition is much greater than the metastable loss rate, then each metastable atom created in the laser beam path is ultimately pumped into the $2p_i$ level. In this situation, the emission rate of the $2p_i$ level is proportional to the rate of electron excitation of metastable level plus the rate of electron excitation of the $2p_i$ level. The emission rate from the latter source can be determined by measuring the emission intensity with no laser excitation. Subtracting this value from the laser-induced signal yields an emission signal proportional to the electron-excitation production rate of the metastable atoms alone. The excitation rate of metastable atoms is proportional to the apparent cross section for excitation of the 1*s* level, $Q^{\mathrm{app}}(1s)$, which is equal to the direct excitation cross section plus the cross section for cascade from all higher levels. Thus the LIF intensity as a function of electron energy gives the relative apparent excitation function for the metastable level. The method for absolute calibration is given in Ref. [7].

In the experiment reported in this paper, an electron beam excites ground-state atoms to various higher levels, resulting in the steady-state densities of the metastable level (level *a*), $n^{\mathrm{init}}(a)$, and the $2p_i$ level (level *b*), $n^{\mathrm{init}}(b)$, which are taken as the "initial" values. Then, a short, powerful laser pulse excites the $a \leftrightarrow b$ transitions and during this pulse the densities of atoms in levels *a* and *b* reach a new dynamic equilibrium:

$$n(a) \approx n(b) \approx \tfrac{1}{2}[n^{\mathrm{init}}(a)+n^{\mathrm{init}}(b)] \approx \tfrac{1}{2}n^{\mathrm{init}}(a) \ . \qquad (1)$$

The last step of the above equation follows from the fact that because of the long lifetime of the metastable atom, the metastable density produced by a steady-state electron beam is much higher than the density of atoms in level *b*. After the cessation of the laser pulse, the level-*b* atoms decay exponentially, eventually reaching the asymptotic value $n^{\mathrm{init}}(b)$. In Fig. 3 we illustrate the time dependence of the $b \rightarrow c$ emission intensity, which is proportional to the instantaneous number density $n(b)$, and for reference the laser pulse is also shown. The integrated intensity signal of the transient $b \rightarrow c$ emission (S_1) is measured over a time interval τ, and after reaching steady state, the integrated $b \rightarrow c$ emission signal (S_2) is measured over the same interval τ. As shown in Sec. II B, the LIF signal S_1-S_2 is proportional to the value of n_b at the end of the laser pulse, i.e., $n^{\mathrm{init}}(a)/2$ according to Eq. (1). Since $n^{\mathrm{init}}(a)$ is directly related to the apparent cross section of the metastable level *a*, measurement of $(S_1$-$S_2)/S_2$ at various electron energies allows us to determine both the metastable number density and the excitation cross section of the metastable level. In the following subsections we show how the LIF signal is related to the metastable number density and cross section and describe methods for absolute measurements.

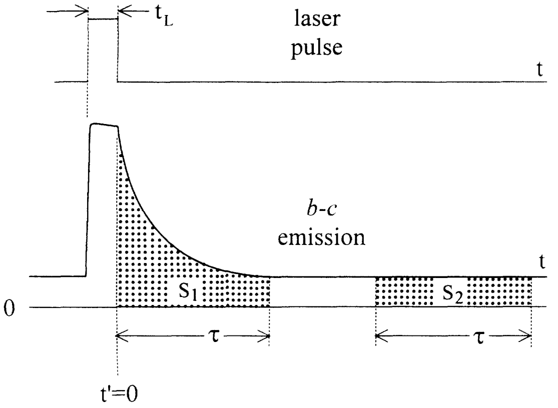

FIG. 3. Time dependence of the $b \rightarrow c$ fluorescence intensity produced by the laser pumping of the metastable atoms. The signal S_1 includes both the transient laser-induced fluorescence and the steady-state emission; S_2 measures only the steady-state signal. The laser pulse is shown at the top of the figure for reference.

B. Quantitative description

In Ref. [7] detailed-balance rate equations are used to analyze the populations of levels a and b in the cw experiment. For very high laser intensities these rate equations may not accurately describe the atomic system populations. This is because if the laser is intense enough to induce many transitions before the upper level spontaneously decays, optical coherences may develop between the laser-connected levels, and the optically pumped atom has to be described as a (partially) coherent superposition of the upper and lower laser-excited states. If coherences exist, the rate equations may not completely describe the atomic system. To analyze coherent systems, one approach is to use the optical analog of the Bloch equations. The Bloch formalism was intended to analyze the two-level system of spin-$\frac{1}{2}$ particles in a magnetic field. By choosing the linear laser polarization to coincide with the quantization axis, only states with the same m_J are coupled by the laser. The atom can then be well approximated as a two-level system and the Bloch formalism applied.

The optical Bloch equations contain not only information about the level populations (like the rate equations), but also information about the components of the atomic dipole moment in phase and in quadrature with the laser field. The relaxation rate of the coherences is governed by spontaneous emission, collisions, and the effect of the inhomogeneous Doppler distribution. If the relaxation rate is sufficiently large, the coherences die away rapidly and the Bloch equations reduce to ordinary rate equations. Although our laser has sufficient total power to cause optical coherences, the multimode nature of the laser prevents optical coherences from developing and allows us to use the rate equation approach (see the Appendix) adopted in this section.

In the absence of the laser beam the only populating mechanism is the electron beam. This rate of increase in the population of state m in level i due to electron excitation (e exc) is

$$\left[\frac{\partial n(i_m)}{\partial t}\right]_{\text{e exc}} = \frac{nj}{e} Q^{\text{app}}(i_m) , \tag{2}$$

where n, j, and e are the ground-level atom density, electron-beam current density, and the electron charge magnitude, respectively, and are constant. The apparent cross section for a Zeeman state m of level i is $Q^{\text{app}}(i_m)$ and the number density of this state is $n(i_m)$. The apparent cross section includes the population of the i_m state by direct electron-impact excitation and by cascade from the higher levels that are also excited by the electron beam. Equation (2) refers to the population rate into a Zeeman state rather than the level as a whole. The cross section of the entire level, $Q^{\text{app}}(i)$, is obtained by summing over all the states within the level, and is the sum of the direct excitation cross section of the level i, $Q^d(i)$, and the cascade from the higher levels j which can be represented by the optical emission cross sections for the $j \rightarrow i$ transitions [9]:

$$\sum_m Q^{\text{app}}(i_m) = Q^{\text{app}}(i) = Q^d(i) + \sum_j Q^{\text{opt}}(j,i) . \tag{3}$$

The sum of the optical cross sections for all emission transitions into level i is the cascade cross section.

The other important nonlaser processes are losses out of the system. For the states of the b level, the dominant loss mechanism is spontaneous emission. For the states of level a, the losses are caused by the migration of the metastable atoms out of the detection system's viewed volume. The rate for both of these processes is written as follows:

$$\left[\frac{\partial n(i_m)}{\partial t}\right]_{\text{loss}} = -A_i n(i_m) , \tag{4}$$

where A_i is the loss rate. These rates are the same for all states within a level.

Before the laser is turned on, the population rate of the electron beam and the loss rate are in equilibrium and the resulting steady-state density of state m in level i is taken as the "initial" value with respect to the LIF experiment, i.e.,

$$n^{\text{init}}(i_m) = \frac{nj}{e} \frac{Q^{\text{app}}(i_m)}{A_i} . \tag{5}$$

Because of the dense mode structure of the dye-laser output, we treat the laser as an intense classical source so that when the laser pulse is introduced, the laser radiation induces emission and absorption between the connected states of the i and j levels at a rate given by

$$\left[\frac{\partial n(i_m)}{\partial t}\right]_{\text{laser}} = \rho(\nu) B [n(j_m) - n(i_m)] , \tag{6}$$

where $\rho(\nu)$ is the laser energy density per unit frequency at frequency ν and B is the induced emission-absorption coefficient for the $j \rightarrow i$ transition such that $B = B_{ji}/3$, where B_{ji} is the standard Einstein induced coefficient. The reason for the factor of one third is that while the Einstein coefficient implicitly includes induced emission into all three linear polarizations, the laser induces emission into only one polarization. Since the rate for each of the three polarizations is equal, B is one third as large as the ordinary Einstein coefficient.

We choose the laser polarization parallel to the direction of the axis of quantization so that only $\Delta m=0$ transitions are induced between levels. The geometry of the LIF interaction region is shown in Fig. 4. The two-level system is described by a pair of equations for each pair of laser-connected states of the same m:

$$\frac{dn(a_m)}{dt}=\frac{nj}{e}\left[Q^{\mathrm{app}}(a_m)-\sum_{m'}Q^{\mathrm{opt}}(b_{m'},a_m)\right]+\rho(\nu)B[n(b_m)-n(a_m)]-A_a n(a_m)+\sum_{m'}A(b_{m'},a_m)n(b_{m'}) , \qquad (7)$$

$$\frac{dn(b_m)}{dt}=\frac{nj}{e}Q^{\mathrm{app}}(b_m)-\rho(\nu)B[n(b_m)-n(a_m)]-A_b n(b_m) , \qquad (8)$$

where $A(b_{m'},a_m)$ is the transition rate from the $b_{m'}$ to the a_m states. The two summation terms in Eq. (7) require an explanation. When there is no laser pumping present, the apparent cross section for state a_m, $Q^{\mathrm{app}}(a_m)$, is sufficient to account for the populating effect of atoms that spontaneously decay from higher levels into state a_m because the apparent cross section includes both direct and cascade contributions as indicated by Eq. (3). When laser pumping is present, however, the population of level b is greatly increased from its initial, steady-state value and consequently the contribution to the population of state a_m from decaying b-level atoms is also increased. We account for this enhanced spontaneous decay contribution to the a_m population by including the last term of Eq. (7) which consists of the $b\rightarrow a$ transition rate times the number density of the initial state summed over all b states that can decay into state a_m. Since we now have included $b\rightarrow a$ decay explicitly, we remove the $b\rightarrow a$ portion of the cascade cross section from $Q^{\mathrm{app}}(a_m)$ as shown in the first square bracket in Eq. (7).

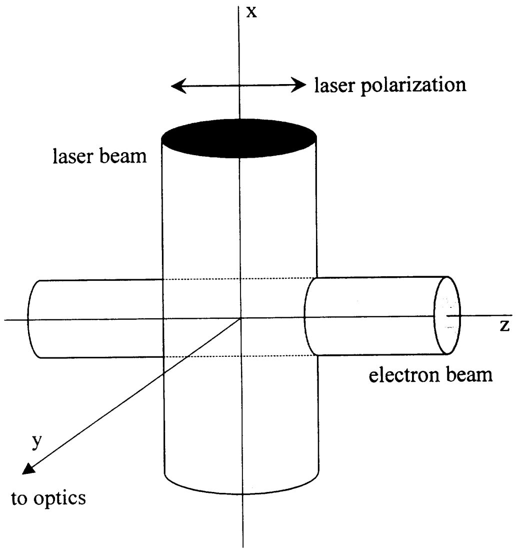

FIG. 4. Geometry of the LIF interaction region for cross-section measurements. The electron beam propagates along the z axis (the quantization axis). The laser beam propagates parallel to the x axis and is linearly polarized along the z axis. The fluorescence is detected along the y axis.

Let us first consider the $1s_3$ metastable level, i.e., $J_a=0$. Dipole selection rules acquire $J_b=1$. Since the laser polarization coincides with the z axis, the b_0 state is pumped by the laser and the b_1 and b_{-1} states are not affected. Accordingly, only one pair of equations ($m=0$) results:

$$\frac{dn(a_0)}{dt}=\frac{nj}{e}\left[Q^{\mathrm{app}}(a_0)-\frac{A_{ba}}{A_b}Q^{\mathrm{app}}(b_0)\right]+\rho(\nu)B[n(b_0)-n(a_0)]-A_a n(a_0)+A_{ba}n(b_0) , \qquad (9)$$

$$\frac{dn(b_0)}{dt}=\frac{nj}{e}Q^{\mathrm{app}}(b_0)-\rho(\nu)B[n(b_0)-n(a_0)]-A_b n(b_0) , \qquad (10)$$

where we have now transformed the optical cross section of Eq. (7) into apparent cross sections in Eq. (9). If we solve Eqs. (9) and (10) and then match the resulting expressions for $n(a_0,t)$ and $n(b_0,t)$ at $t=0$ (the instant the laser turns on) to the initial densities of Eq. (5), the exact solution for the number density in state b_0 at time t while the laser is on is

$$n(b_0,t)=n^{\infty}(b_0)[1-e^{r_2t}]+njQ^{\mathrm{app}}(b_0)(2eA_b)^{-1}[e^{r_2t}+e^{r_1t}]+nj(2e)^{-1}\{Q^{\mathrm{app}}(a_0)A_a^{-1}+Q^{\mathrm{app}}(b_0)[\rho(\nu)B]^{-1}\}[e^{r_2t}-e^{r_1t}] , \qquad (11,$$

where r_1 and r_2 satisfy a quadratic equation whose solutions are well approximated by

$$r_1\approx-2\rho(\nu)B \quad\text{and}\quad r_2\approx-(A_a+A_b-A_{ba})/2 \qquad (12)$$

and

$$n^{\infty}(b_0)=\frac{nj}{e}\,\frac{Q^{\mathrm{app}}(b_0)A_a+\rho(\nu)B[Q^{\mathrm{app}}(b_0)(1-A_{ba}/A_b)+Q^{\mathrm{app}}(a_0)]}{\rho(\nu)B(A_a+A_b-A_{ba})+A_aA_b} , \qquad (13)$$

which is the steady-state solution to Eq. (10) and is the resulting population of level b when pumped by a cw laser.

Equation (11) is further simplified in the case of a very short, high-intensity laser pulse. Let us consider this limiting case for a laser pulse of length t_L small enough that $e^{r_2 t_L} \approx 1$, an energy density $\rho(\nu)$ large enough that $e^{r_1 t_L} \approx 0$, and $\rho(\nu)B \gg A_a$. The result is now simplified to

$$n(b_0, t=t_L) = \frac{1}{2}\frac{nj}{e}\left[\frac{Q^{\text{app}}(b_0)}{A_b} + \frac{Q^{\text{app}}(a_0)}{A_a}\right], \tag{14}$$

which is the average of the $n^{\text{init}}(b_0)$ and $n^{\text{init}}(a_0)$, as can be seen from Eq. (5). This suggests a more intuitive interpretation of our solution: before any other processes occur, the populations of states a and b will redistribute themselves to be in equilibrium with the laser as signified by Eq. (1) in the qualitative discussion of this experiment. For this laser polarization the two laser-connected states share their total population equally, just as predicted by the Bloch solution (see the Appendix).

Although our laser energy is large enough to make $e^{r_1 t_L} \approx 0$ and $\rho(\nu)B \gg A_a$ valid (see Sec. IV B), the pulse length is somewhat too long for $e^{r_2 t_L} \approx 1$ to hold true so we must carry the exponential terms along.

After turning off the laser at $t=t_L$, the population of state b_0 will vary in time as

$$n(b_0, t) = n_0 \exp[-A_b(t-t_L)] + (nj/e)Q^{\text{app}}(b_0)A_b^{-1}, \quad t > t_L \tag{15}$$

which is the solution of rate equation (10) when $\rho(\nu)=0$. If we let

$$t' = t - t_L \tag{16}$$

and match Eq. (11) to Eq. (15) at $t'=0$, we get

$$\begin{aligned} n_0 &= n(b_0, t'=0) - nje^{-1}Q^{\text{app}}(b_0)A_b^{-1} \\ &= \{n^{\infty}(b_0)(1-e^{r_2 t_L}) \\ &\quad + \tfrac{1}{2}(nj/e)e^{r_2 t_L}[Q^{\text{app}}(a_0)A_a^{-1} + Q^{\text{app}}(b_0)A_b^{-1}]\} \\ &\quad - (nj/e)Q^{\text{app}}(b_0)A_b^{-1}. \end{aligned} \tag{17}$$

When we measure the emission signal due to the $b \to c$ decay experimentally, we observe the emission due to the decay of all of the b states, regardless of whether or not they are pumped by the laser. In this instance we add the contribution of the $m=\pm 1$ states of the b level to arrive at the total number of atoms in the whole of level b:

$$\begin{aligned} n(b, t') &= n(b_0, t') + (nj/e)[Q^{\text{app}}(b_1)A_b^{-1} + Q^{\text{app}}(b_{-1})A_b^{-1}] \\ &= \left\{n^{\infty}(b_0)(1-e^{r_2 t_L}) + \frac{nj}{2e}e^{r_2 t_L}\left[\frac{Q^{\text{app}}(a_0)}{A_a} + \frac{Q^{\text{app}}(b_0)}{A_b}\right] - \frac{nj}{e}\frac{Q^{\text{app}}(b_0)}{A_b}\right\}e^{-A_b t'} + \frac{nj}{e}\frac{Q^{\text{app}}(b)}{A_b}. \end{aligned} \tag{18}$$

The emission signal detected in a time τ, $\tau \gg A_b^{-1}$, from within a viewed volume V and in a direction perpendicular to the electron beam is

$$S_1 = \varepsilon(\lambda)(1-P/3)^{-1} A_{bc} \int_V \int_0^{\tau} n(b, t')\,dt'\,d^3x, \tag{19}$$

where P is the polarization of the emission and $\varepsilon(\lambda)$ is the photon detection efficiency of the apparatus at wavelength λ. This efficiency factor includes the geometry, reflection, and transmission coefficients of the optical components, as well as the absolute efficiency of the detector. Looking at Eq. (18), we see that the only spatially dependent portion of $n(b,t')$ is the electron beam current density j. In Eq. (19) then, the integral of j over the volume is the total electron beam current I times the length of the electron beam viewed by the monochromator entrance slit width w, provided that the viewed volume encompasses the entire radial extent of the electron beam. This leads to

$$\begin{aligned} S_1 &= \varepsilon(\lambda)\frac{1}{(1-P_{\text{LIF}}/3)}\frac{A_{bc}}{A_b}\left\{n^{\infty}(b_0)(1-e^{r_2 t_L}) + \frac{nIw}{2e}e^{r_2 t_L}\left[\frac{Q^{\text{app}}(a_0)}{A_a} + \frac{Q^{\text{app}}(b_0)}{A_b}\right] - \frac{nIw}{e}\frac{Q^{\text{app}}(b_0)}{A_b}\right\} \\ &\quad + \varepsilon(\lambda)\frac{1}{(1-P_{\text{ss}}/3)}\frac{A_{bc}}{A_b}\frac{nIw}{e}Q^{\text{app}}(b)\tau. \end{aligned} \tag{20}$$

Because the laser beam may populate the b states differently from the steady-state electron beam, we distinguish the polarization correction for the transient fluorescence, P_{LIF}, in the first half of the preceding expression for S_1 from the polarization correction associated with the steady-state emission P_{ss}. After the laser-induced fluorescence is gone, the steady-state $b \to c$ emission signal detected in time τ is

$$S_2 = \varepsilon(\lambda)(1-P_{\text{ss}}/3)^{-1} A_{bc} \int_V \int_0^{\tau} \frac{nj}{e}\frac{Q^{\text{app}}(b)}{A_b}\,dt'\,d^3x = \varepsilon(\lambda)(1-P_{\text{ss}}/3)^{-1}\frac{A_{bc}}{A_b}\frac{nIw}{e}Q^{\text{app}}(b)\tau. \tag{21}$$

The LIF signal S_{LIF} is equal to $S_1 - S_2$ so that

$$\begin{aligned} S_{\text{LIF}} &= \varepsilon(\lambda)(1-P_{\text{LIF}}/3)^{-1} A_{bc} A_b^{-1} \\ &\quad \times \left\{n^{\infty}(b_0)(1-e^{r_2 t_L}) + \tfrac{1}{2}(nI/e)we^{r_2 t_L}[Q^{\text{app}}(a_0)A_a^{-1} + Q^{\text{app}}(b_0)A_b^{-1}] - \frac{nIw}{e}Q^{\text{app}}(b_0)\right\}. \end{aligned} \tag{22}$$

It can be shown that the $n^{\infty}(b_0)$ term is approximately three orders of magnitude smaller than the other terms in Eq. (22). Similarly, since $A_a \ll A_b$, the $Q^{\mathrm{app}}(a_0)A_a^{-1}$ term will also dominate the $Q^{\mathrm{app}}(b_0)A_b^{-1}$ terms by several orders of magnitude, and for a $J_a=0$ level $Q^{\mathrm{app}}(a_0)=Q^{\mathrm{app}}(a)$, we get

$$S_{\mathrm{LIF}}=\varepsilon(\lambda)\frac{1}{(1-P_{\mathrm{LIF}}/3)}\frac{e^{r_2 t_L}}{2}\frac{A_{bc}}{A_b}\frac{nIw}{e}\frac{Q^{\mathrm{app}}(a)}{A_a} . \tag{23}$$

Clearly, S_{LIF} is proportional to the metastable apparent cross section $Q^{\mathrm{app}}(a)$.

For the $1s_5(J_a=2)$ metastable level, J_b is not limited to one value. If we chose $J_a=2 \rightarrow J_b=1$, only three of the five metastable states are connected to the b states by the laser. We can analytically solve the three pairs of equations arising in this case so long as the b state densities remain approximately equal to each other during the laser pulse. This condition allows us to decouple the pairs of equations from each other and obtain solutions very similar to Eq. (11) for each pair of equations. Even if this condition is not satisfied, the coupling is extremely small and our numerical work indicates that this has a negligible effect on the solution. In their LIF experiment, Phelps *et al.* [10] found that the cross sections for electron excitation into all five Zeeman states of the $1s_5$ level of Ne at 18.2 eV are identical within experimental uncertainty. In this regard it is interesting to note that the calculations of Zhang, Sampson, and Clark [11] indicate that the collision strengths for electron excitation into the magnetic sublevels within a $J=1$ manifold are nearly identical for a number of excited configurations of the neonlike iron ion. If we assume that the Ar metastable state densities are equal initially ($t=0$), the resulting expression for S_{LIF} for the $J_a=2 \rightarrow J_b=1$ case is the same as Eq. (23) except for a multiplicative factor of $\frac{3}{5}$ on the right-hand side to compensate for the unpumped a states ($m_a=\pm 2$). If the metastable states are not equally populated by the electron beam, then the compensating factor for the unpumped states is the ratio of the sum of the densities of the laser-connected metastable states ($m=0$ and $m=\pm 1$) to the sum of the densities in all five states. If we pump $J_a=2 \rightarrow J_b=2$, four of five of the metastable states are connected by the laser to the b manifold (the dipole matrix element connecting $J_a=2$, $m_a=0$ to the $J_b=2$, $m_b=0$ states is zero). We can solve the four pairs of equations arising in this case and obtain a solution like Eq. (23) except for a similar compensating factor equal to the ratio of the densities of the laser-connected metastable Zeeman states ($m=\pm 1$ and $m=\pm 2$) to the sum of the densities on all five states. This factor is $\frac{4}{5}$ when all five Zeeman states have equal initial populations. When the laser is tuned to pump the $J_a=2 \rightarrow J_b=3$ transition, all five of the Zeeman states of the metastable level are pumped into level b so that there is no compensating factor required.

By choosing the laser polarization as our quantization axis, the laser coupling of the levels reduces to essentially a two-level problem that is analytically solvable. To describe the system more generally requires a density-matrix approach to account for the Zeeman coherences that arise when the laser polarization and the quantization axis do not coincide. We have developed such a theoretical description which allows us to analyze the system for an arbitrary laser polarization. When the laser polarization is chosen along the quantization axis, the results are identical to those in this paper.

C. Applications

Equation (23) indicates that the LIF signal is proportional to the apparent excitation cross section of the metastable atom. This allows us to determine the cross sections for excitation into the metastable levels from the LIF signal produced by a pulsed laser, just like the use of the cw LIF scheme in Ref. [7]. In addition, we note that $Q^{\mathrm{app}}(a)/A_a$, times the constant (nI/e) which appears in Eq. (23), is related to the number density of the metastable atoms produced by an electron beam. Thus it is possible to use the pulsed LIF technique to determine both the excitation cross section of the metastable levels and the number density of the metastable atoms, in contrast to the cw LIF experiments which yield the cross sections but not the number density. The methods for using the pulsed LIF to determine the cross section and number density, including the method of absolute calibration, are described in the following subsections. Another application of the pulsed LIF technique is the measurement of the temporal metastable density in a time-dependent system. Since the laser pulse width is on the order of nanoseconds, one can use this technique to measure, for example, the disappearance rate of the metastable atoms as described in Sec. II C 3, provided that the disappearance time constant is much larger than the laser pulse width.

1. Measurement of absolute metastable cross sections

From Eq. (23) and our experimental results we obtain the energy dependence of the apparent metastable cross section $Q^{\mathrm{app}}(a)$. It still remains to determine the absolute magnitude of $Q^{\mathrm{app}}(a)$ and to extract the direct cross section $Q^{d}(a)$ from $Q^{\mathrm{app}}(a)$ according to Eq. (3). The only remaining unknown variables in Eq. (23) are A_a and $\varepsilon(\lambda)$. Instead of determining A_a directly, we rely on the calibration technique developed for the cw experiment of Ref. [7].

The $1s_3$ and $1s_5$ metastable levels are of purely triplet character [5,7,9]. Because of their spin-changing nature, the cross sections for direct excitation from the $^1S_0$ ground level to the $1s_3(^3P_0)$ or $1s_5(^3P_2)$ levels peak at an energy slightly above threshold and diminish rapidly with increasing incident electron energy. Nearly all of the levels cascading into the metastable atoms have some singlet admixture to their wave functions so that the cross sections for exciting these cascading levels do not decrease as rapidly with increasing electron energy as do the cross sections for nearly pure triplet metastable levels [5,7]. At large energies (> 80 eV) the direct cross section into the $1s_3$ or $1s_5$ levels is negligible compared to the total cascade cross section and so at these energies the apparent cross section is essentially equal to the total cascade cross section. Indeed, above electron energies of 90 eV the energy dependence of our $1s_3$ and $1s_5$ apparent cross sections agrees very well with that of the total cascade cross section above electron energies of 90 eV. By setting the apparent excitation cross section equal to the absolutely measured cascade cross-section curve at high energies, we calibrate the metastable apparent cross section. Not only does this method put our metastable apparent cross section on an absolute scale, but it provides the absolute size of the direct cross section as well: the difference between the curves at low energies is due entirely to direct excitation into the metastable level. This procedure does not give the direct cross sections for energies above 90 eV. This is a consequence of the intrinsic difficulty of determining direct excitation cross sections by the subtraction of the cascade cross section from the apparent cross section when the direct cross section is much smaller than the cascade contribution.

2. *Absolute metastable number density*

We also measure the number density of the metastable atoms using the same LIF procedure. Instead of integrating Eq. (19) over the entire radial extent of the electron beam in order to obtain Eq. (20), which relates the observed signal to $Q^{\mathrm{app}}(a_0)$, here we focus on a small volume ΔV within the electron beam because of the radial dependence of $n^{\mathrm{init}}(a)$ in the cylindrical geometry. If we observe the $b \rightarrow c$ fluorescence originating from the small volume ΔV with the laser on (S_1') and off (S_2'), the difference between S_1' and S_2' gives the LIF signal, analogous to Eq. (23), as

$$S'_{\mathrm{LIF}} \approx \varepsilon(\lambda)(1-P_{\mathrm{LIF}}/3)^{-1} e^{r_2 t_L} \frac{1}{2} \frac{A_{bc}}{A_b} \int_{\Delta V} n^{\mathrm{init}}(a)\, d^3x \ . \tag{24}$$

If ΔV is limited to a small enough region inside the electron beam, it is reasonable to assume that the current density and thus $n^{\mathrm{init}}(a)$ are constant within this volume. Then the integral over the volume can be simplified to $n^{\mathrm{init}}(a)\Delta V$. This volume's bounds are delineated by the diameter of the laser beam and an auxiliary horizontal slit placed immediately in front of the monochromator entrance slit. The resulting volume is a short, right circular cylinder at the center of the electron beam, oriented perpendicular to it, as illustrated in Fig. 5.

For absolute measurement of $n^{\mathrm{init}}(a)$, it is convenient to eliminate $\varepsilon(\lambda)$ in Eq. (24) by means of Eq. (21) so as to express the metastable number density in terms of the $b \rightarrow c$ optical emission cross section, i.e.,

$$n^{\mathrm{init}}(a) = \frac{S'_{\mathrm{LIF}}}{S_2} \left[\frac{1-P_{\mathrm{LIF}}/3}{1-P_{\mathrm{ss}}/3} \right] e^{-r_2 t_L} \times 2 \frac{nI}{e} \frac{A_b}{A_{bc}} Q^{\mathrm{opt}}(b,c) \frac{\tau w}{\Delta V} \mathcal{C} \ , \tag{25}$$

where the ground level density n and the electron beam current I are the values when measuring S_2. The static gas target density n is easily determined by a capacitance manometer (see Sec. III A). We have replaced the apparent cross section for level b, $Q^{\mathrm{app}}(b)$, with the optical cross section for the $b \rightarrow c$ transition times the inverse of the $b \rightarrow c$ branching ratio (A_b/A_{bc}). The factor $\mathcal{C}$ compensates for the a states unpumped by the laser (see Sec. II B). To determine the number densities resulting from the laser pumping for either $J_a=0 \rightarrow J_b=1$ or $J_a=2 \rightarrow J_b=3$, $\mathcal{C}=1$ in Eq. (25) because all of the states within the metastable level are pumped by the laser. If we choose $J_a=2 \rightarrow J_b=1$ or 2, not all of the metastable states are pumped by the laser so $\mathcal{C}>1$ to account for the unpumped states. In the case of $J_a=2 \rightarrow J_b=1$ the laser samples only the $m_J=0,\pm1$ states and the compensating factor is the ratio of the total population of all five states to the population of these three pumped states. If the initial populations of the Zeeman states of the metastable level are equal, then $\mathcal{C}=\frac{5}{3}$ for the $J_a=2 \rightarrow J_b=1$ case and $\mathcal{C}=\frac{5}{4}$ for the $J_a=2 \rightarrow J_b=2$ case.

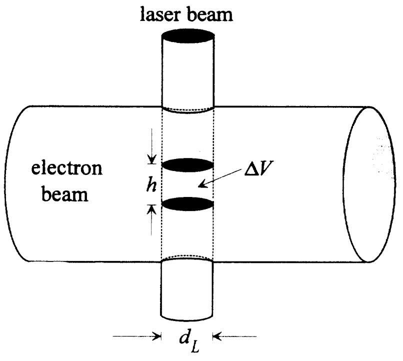

FIG. 5. Geometry of the LIF interaction region for absolute number density measurements. This figure is similar to Fig. 4, except that the laser beam diameter (d_L) is smaller than that of the electron beam. The observed volume is further reduced to a height h by an auxiliary horizontal slit placed at the entrance slit of the monochromator.

3. *Disappearance rates of the metastable atoms*

In the experiment described in Sec. II C 2, we measured the number density of the metastable atoms produced by a steady-state electron beam. If we turn off the electron beam and a short time later trigger the laser pulse to measure S'_{LIF}, we can examine how many metastable atoms remain relative to the number measured when the beam is on. By probing with the laser at a variety of delay times after the electron beam cutoff, we can map the temporal decrease in the number of metastable atoms in the absence of the electron beam. The relatively short laser pulse width of the laser (10 ns) makes it well suited for obtaining the disappearance plot of the metastable atoms. Measurements of disappearance rates require only relative number densities without absolute calibration which greatly simplifies the experimental procedure.

III. EXPERIMENTAL APPARATUS

In the LIF experiment a collimated, monoenergetic electron beam passes through the ground level argon atoms, producing metastable atoms (level a in Fig. 2). A pulsed laser beam intersects this electron beam at right angles and pumps the metastable atoms from level a to level b. The additional transient radiation from these atoms spontaneously decaying from level b to level c is observed in the direction perpendicular to both the laser and electron beams. The intensity of this transient $b \rightarrow c$ emission is proportional to the apparent metastable cross section $Q^{\mathrm{app}}(a)$ and the steady-state initial metastable number density $n^{\mathrm{init}}(a)$. The absolute calibrations of $Q^{\mathrm{app}}(a)$ and $n^{\mathrm{init}}(a)$ require auxiliary experiments that measure a series of absolute optical emission cross sections, e.g., the cross sections for cascade into the a level and $Q^{\mathrm{opt}}(b,c)$, as explained in Secs. II C 1 and II C 2. Two types of apparatus are used in this paper: one for the LIF measurements and another to measure the absolute optical emission cross sections.

A. LIF system

The experimental apparatus can be divided into four principal parts: the vacuum system, the electron gun, the laser system, and the fluorescence detection system. A block diagram of the apparatus is shown in Fig. 6. The vacuum system consists of a stainless-steel chamber with metal gaskets, evacuated by a diffusion pump and using an ion pump for long-term pressure maintenance. The ultimate pressure is better than 1×10^{-7} Torr. For this experiment we admit 3 mTorr of Ar to the evacuated chamber; the Ar pressure and thus the ground level density is determined by a capacitance manometer to better than 1% accuracy. The manometer signal is monitored by the computer via an analog-to-digital (A-D) port. A getter pump operates during data collection, eliminating any atmospheric gases that might leak into the chamber but leaving the Ar density unaffected. Pressure stability is excellent: we observe a less than 2% change in pressure over a 12-h period. Magnetic shielding inside the collision chamber minimizes the penetration of the earth's magnetic field into the interaction region.

The electron gun is a pentode type with electrostatic focusing elements similar to the one used in Ref. [12]. This design produces an electron beam 2–3 mm in diameter and with a total current of 50 to 500 μA over the energy range 10–200 eV. The energy spread of the beam is typically 0.5 eV (FWHM), measured by observing the spread in the onset of an excitation function.

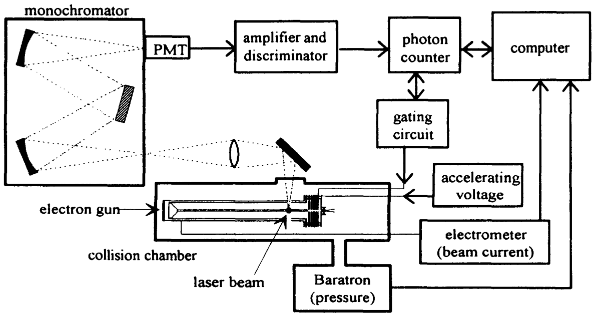

FIG. 6. Block diagram of the experimental apparatus used for the LIF measurements.

The collision region is inside a grounded Faraday cup which is itself inside a grounded shield. Vertical slits in the sides of the cup and shield allow the Ar radiation to reach the detection optics. These slits are roughly five times as wide as the viewed width of the electron beam. The vertical extent of the Faraday cup slits permits us to collect the radiation from relatively long-lived levels that might migrate out of the electron beam proper. Small apertures in the top and bottom of the cup and shield allow the laser beam to pass through the collision region. Previous work [7] has shown that much less than 1% of the total electron beam current escapes undetected through these openings in the Faraday cup. An electrometer measures the total electron beam current and provides an output for an A-D port of the computer.

The laser system is composed of a tunable dye laser pumped by the second harmonic of a pulsed 20-Hz Nd:YAG (where YAG denotes yttrium aluminum garnet) laser (532 nm). We use LDS700 laser dye dissolved in methanol to pump the $1s_5$-$2p_2$ (696.5 nm) and $1s_5$-$2p_3$ (706.7 nm) transitions. For the $1s_3$-$2p_2$ and $1s_5$-$2p_7$ transitions (772.4 nm), we use LDS751 in dimethyl sulfoxide (DMSO). The bandwidth of the dye laser is about 0.05 nm and the pulse duration is 10 ns. Typical output power is 1–3 mJ/pulse which is well above the minimum saturation density (see Sec. IV). We tune the dye laser to the desired transition wavelength by using the optogalvanic signal from a hollow cathode Ar discharge lamp.

The LIF detection system consists of a monochromator, a photomultiplier tube (PMT), photon-counting electronics, a gate generator, and a personal computer. An achromat lens focuses the fluorescence at 1:1 magnification onto the entrance slit of a Jobin-Yvon 1-m monochromator. The width of the monochromator entrance slit defines the viewed segment of the electron beam. The $b \rightarrow c$ emission that we isolate with the monochromator is chosen to have a different wavelength than the $a \rightarrow b$ transition pumped by the dye laser so as to minimize the detection of scattered laser light. An RCA model C31034A-02 (GaAs-type) PMT in a photon-counting mode at the exit slit detects the dispersed radiation. The raw fluorescence signal S_1 for the $b \rightarrow c$ transition collected in a short gate opening immediately on the trailing edge of the laser pulse consists of the signals from the transient LIF (S_{LIF}) and from the steady-state electron beam excitation (S_2). The latter is collected in an identical-length gate a long time (1.5 msec) after the laser pulse and subtracted from S_1 to give S_{LIF} (see Fig. 3). The gate lengths we use range from 1.3 to 2.1 μsec, more than 20 times the lifetime of any of the $b \rightarrow c$ transitions we study and so sufficiently long to collect all of the transient fluorescence. A p-i-n diode detects the laser pulse as it exits the chamber and sets the timing for the detection gates.

The PMT also detects a small amount of scattered laser light along with the LIF signal. By collecting data ($S_1 - S_2$) at the beginning of a run at an electron energy below the threshold of excitation into the metastable levels, we determine the amount of this scattered light subtracted from the raw fluorescence signal. We typically collect 2000–3000 gate pairs for each data point. The computer scans the entire electron energy range in preset discrete steps. To help reduce any systematic long-term drift-induced errors, we scan the energy range seven to ten times. In this way the LIF signal at a particular energy is composed of approximately 2×10^4 gate pairs distributed in time throughout the run.

B. Systems for measuring absolute cascade and emission cross sections

There are two parts to the emission cross-section measurement. First, we determine the energy dependence of the relative emission cross section for all transitions cascading into each of the $1s_3$ and $1s_5$ levels [to calibrate $Q^{\text{app}}(a)$] and the energy dependence of the $Q^{\text{opt}}(b,c)$ [to calibrate $n^{\text{init}}(a)$]. Second, we measure the absolute emission cross section for these transitions at the peak of the energy dependence (22 eV). We measure the energy dependence of the individual cascade cross sections with the same apparatus used to collect the LIF data. The absence of the laser beam is the only difference from Fig. 6. For these measurements, the electron beam is modulated; one 99.9-μsec gate opens while the electron beam is on to collect the photons from the transition of interest, then the electron beam is turned off and a second 99.9-μsec gate collects stray background light. The difference between the counts in the two gates divided by the electron beam current is proportional to the cross section. Similar to the case for LIF data collection, we traverse the electron energy range of the transition from threshold to 200 eV in discrete steps, at each step collecting some 4×10^4 gate pairs. The energy range is covered five to ten times. The computer collects the results from the photon counters, monitors the electron beam current and gas pressure, controls the electron energy, and analyzes and stores the data.

To measure the absolute cascade cross sections, we use a method and an apparatus described fully in Ref. [12]. The apparatus is similar to the one shown in Fig. 6. The significant differences, besides the absence of the laser, are a SPEX 1.26-m monochromator in place of the Jobin-Yvon 1-m monochromator and an all-reflective optical system. We use the PMT (RCA model C31034A-02 or Hamamatsu model 7102) in an analog mode and run the output through a lock-in amplifier in conjunction with a mechanical chopper. The amplifier output feeds into a strip chart recorder that records the spectrum as the monochromator scans across the transitions. We determine the absolute photon detection efficiency of the system and thus the absolute cascade cross sections by effectively replacing the electron beam emission with that of a standard lamp of known spectral irradiance.

IV. RESULTS AND DISCUSSION

A. Cascade cross sections

At electron energies above about 90 eV, the metastable apparent cross section is due almost entirely to cascade since the direct excitation cross section, as explained in Sec. II C, is negligible in comparison with the cascade. Even at lower energies, the cascade contribution to the apparent cross section is very large. According to Ref. [6], the dominant cascade contributors to the Ar metastable levels are from the $3p^54p$ manifold ($2p_1$ through $2p_{10}$ in Paschen's notation). The contributions of these levels to the total cascade cross section comprise more than 99% of the cascade into the $1s_3$ level and 98% of the cascade into the $1s_5$ level. The $3p_9(J=3)$ level of the $3p^55p$ manifold is the only other significant cascade contributor. With the exception of the $2p_9$ and $3p_9$ levels, which have purely triplet character, the cascading levels are described by linear superpositions of triple and singlet wave functions. It is the presence of this singlet component that prevents the cascade cross sections from decreasing too rapidly with electron energy and allows us to distinguish the cascade excitation function from that of the purely triplet metastable levels and hence enables us to calibrate absolutely the metastable cross sections.

In general, the Ar cascade cross sections exhibit a distinct peak at about 22 eV and fall to 5% to 50% of their peak value by 200 eV. All of these transitions are found to exhibit varying degrees of pressure dependence in the shapes of the excitation function and in the peak magnitude of the ratio of the signal to pressure. At the peak value this dependence is manifest in a quadratic component in the relationship between signal and pressure, resulting in seemingly larger "cross sections" at higher pressures. Our investigations indicate that the nonlinearity ranges from 1.2% to 7.5% per mTorr for the prominent cascade transitions (e.g., at 1 mTorr the cross section is 1.2% to 7.5% higher than the nominal value). At higher electron energies the signal exhibits a larger quadratic component in its pressure dependence, often twice as large as that at the peak energy. These varying degrees of pressure dependence at different energies produce an overall change in the shape of the excitation function as the pressure increases: at higher pressures the high-energy tail tends to increase with respect to the peak value. Because of the dependence of the excitation function shape on pressure, we remeasured all of the $2p_i\rightarrow1s_3$ and $np_i\rightarrow1s_5$ excitation functions and absolute cross sections to ensure that the cascade cross sections for the metastable levels were measured at the same pressure that the LIF data were taken. For the same reason we have also measured the absolute emission cross section for the $b\rightarrow c$ transition that we use to calibrate the absolute number density measurement.

These pressure effects are not completely understood, but they are likely to be due in part to cascade into the $2p$ levels from $3p^5ns(J=1)$ and $3p^5nd(J=1)$ levels which are optically connected to the ground level. As these higher levels initially decay, a percentage will return to the ground level and another portion will decay to a $2p$ level in accordance with the branching ratios. The radiation from atoms decaying to the ground level has a possibility of being reabsorbed by a ground level atom and the resulting excited atom once again has an opportunity to decay to a $2p$ level. As the gas density increases, the radiation trapping increases, thus causing a nonlinear relationship between the cascade population of the $2p$ levels and the pressure. These resonant levels from the $3p^5ns$ and $3p^5nd$ configurations generally have very broad excitation functions: between 70 and 200 eV the cross sections of these levels typically remain within 80% of the peak value. Since an increase in pressure increases the percentage contribution of the cascade from these levels into the $2p$ manifold, there is a pressure-dependent behavior of excitation cross-section data of the $2p$ levels. Further study, however, is necessary to reach a more detailed understanding of these pressure effects.

As explained earlier, in this experiment we measure the $2p_i \rightarrow 1s_3$ and $2p_i \rightarrow 1s_5$ emission cross sections to obtain the total cascade cross sections into the $1s_3$ and $1s_5$ levels in order to provide an absolute calibration to the relative apparent cross sections for these two levels determined by the LIF measurements. For this purpose it is not necessary that the cascade cross sections be measured at the very low pressure regime. So long as both the LIF and cascade cross-section measurements are taken at the same pressure, the absolute calibration is not affected by the nonlinear pressure dependence of the cascade radiation signal. Thus for each set of the LIF data, we always measure the cascade cross sections over the energy range 10 to 200 eV at the same pressure. As discussed in Sec. IV B 2, we find no discernable difference in the *direct* excitation cross sections for the $1s_3$ and $1s_5$ levels deduced from LIF data taken at pressures ranging from 3 to 11 mTorr. All of the cross-section data presented in this paper were taken at pressures between 2.9 and 3.1 mTorr. This pressure regime was chosen to be low enough to minimize pressure effects and yet high enough to give us a good signal-to-noise ratio. We have also verified that the cascade cross sections are independent of electron-beam current in our experimental regime of 20 to 500 μA.

With the exception of the $2p_9$ and $2p_{10}$ levels, our measurements of the cascade cross sections generally agree well with those of Ref. [6]. Our $2p_9$ cross-section measurement at 100 eV agrees very well with that of Ref. [6] but our excitation function is somewhat less sharply peaked than theirs, resulting in a lower cross section at 22 eV. The $2p_{10}$ cross sections of Ref. [6] are nearly twice as large as ours, and we have no explanation for this discrepancy. We also measure the excitation functions for the cascading levels at 3.0 ± 0.1 mTorr. The excitation functions contributing most significantly to the total cascade cross sections of the $1s_3$ and $1s_5$ metastable levels are presented in Fig. 7. In the case of the $1s_3$ level, the $2p_4$ level alone comprises 60% of the total into the level at the peak value of the cross section. For the $1s_5$ levels, cascade from the $2p_{10}$, $2p_9$, and $2p_6$ levels accounts for more than 80% of the total. We estimate the uncertainty for the total of the cascade cross sections to be ±15% for the $1s_3$ level and ±20% for the $1s_5$ level.

B. LIF measurements

1. *Laser saturation and geometry considerations*

To arrive at the proportionality between S_{LIF} and $Q^{\mathrm{app}}(a)$ in Eq. (23), we assumed that $e^{r_1 t_L} \approx 0$, where r_1 was dependent on the laser energy density. If we require $e^{r_1 t_L} \le 0.001$ and use the relevant values for the $1s_3$-$2p_2$ transition, we find that the required laser energy is less than 1 μJ/pulse: roughly 10^3 smaller than our typical dye-laser power. Physically, this approximation is equivalent to saturating the transition completely. To verify this, we calculate the full width at half maximum (FWHM) of the hole, $\Delta\nu_{\mathrm{hole}}$, burned in the Doppler-broadened atomic line shape $\Delta\nu_D$. For complete saturation, $\Delta\nu_{\mathrm{hole}}$ must encompass $\Delta\nu_D$. For a single-mode laser, the width of this power-broadened hole is given by

$$\Delta\nu_{\mathrm{hole}} = \Delta\nu_{\mathrm{homo}}(1 + I_\nu I_s^{-1})^{1/2} , \tag{26}$$

where $\Delta\nu_{\mathrm{homo}} = A_{ba}/2\pi$ is the homogeneous linewidth of the transition. The laser intensity is I_ν and I_s is the optical saturation pumping parameter [13] $I_s = h\nu(\sigma_{\mathrm{abs}} t_L)^{-1}$, where $\sigma_{\mathrm{abs}} = (\lambda^2 g_b)/(2\pi g_a)$ is the cross section for stimulated absorption taken at the center of the homogeneous, radiatively broadened line shape and g_a and g_b are the statistical weights of the levels. If the laser mode is tuned to the center of the Doppler profile, the width of the power-broadened hole would need to be the same as the Doppler width,

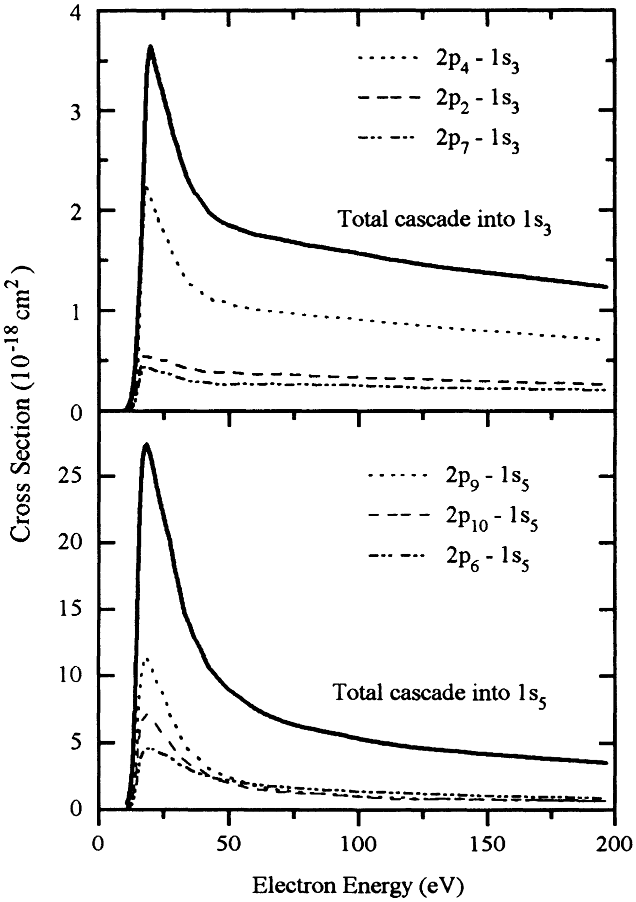

FIG. 7. Plots of the total cross sections for cascade into the $1s_3(J=0)$ and $1s_5(J=2)$ metastable levels versus incident electron energy. Also shown are the most significant contributing $2p_i \rightarrow 1s_3$ and $2p_i \rightarrow 1s_5$ optical cross sections. The cascade shown here corresponds to the second term of Eq. (3).

$$\Delta\nu_D = \nu[(8kT\ln 2)/(mc^2)]^{1/2} = 8\times 10^8\ \text{Hz}\ .$$

This requires $I_\nu = 5\times 10^6\ \text{W m}^{-2}$. The precise nature of our dye laser's mode structure is difficult to characterize. There are hundreds of longitudinal modes within the bandwidth of the dye laser. From shot to shot, different subsets of the available modes lase. We can measure power and spectral profile only by averaging over many shots and in this way we find the total power to be $5\times 10^9\ \text{W m}^{-2}$ per pulse and the bandwidth to be 30 GHz (FWHM). Within the central 4 MHz of the dye-laser spectral distribution, the average power is $625\times 10^6\ \text{W m}^{-2}$. If any one of the many modes within this spectral range lases, it would have sufficient power to saturate the transition, even if it were far from the center of the Doppler distribution. In the more likely event of more than one mode lasing, the combination of modes also has more than sufficient power to saturate the transition.

Although it is important that our laser power density is large enough to completely saturate the transition, it is equally important that the power density be below the threshold for multiphoton ionization-excitation of the metastable atoms. Experimentally, the complete saturation of the transition is indicated by the independence of S_{LIF} from the dye-laser intensity for intensities above saturation. Multiphoton excitation causes a reduction in the LIF signal as the laser intensity is increased and begins to pump atoms out of the *a*-*b* system. Figure 8 shows S_{LIF} plotted for a range of dye-laser intensities. The signal is clearly independent of the laser power in our experimental regime and shows no indication of multiphoton processes.

To verify further that the approximations used in the derivation of Eq. (23) are valid, we have measured the apparent excitation function for the $1s_5$ metastable level of Ne and have compared it to the cw laser result of Ref. [7]. The excitation function shapes obtained using the pulsed laser are identical to those measured with the cw laser, further confirming that $S_1 - S_2$ is proportional to the apparent metastable cross section when using the pulsed laser.

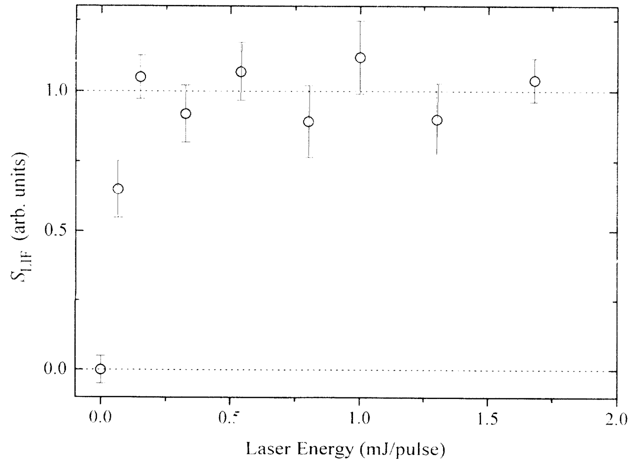

FIG. 8. Plot of S_{LIF} versus laser energy. Here the $1s_3$ metastable atoms are pumped to the $2p_2$ level and the $2p_2 \rightarrow 1s_2$ fluorescence is observed. Above 0.13 mJ/pulse, the signal remains constant, demonstrating saturation. The pulse length is 10 nsec and the laser beam diameter is 5 mm.

Another experimental consideration for cross-section measurements is that the electron beam diameter must remain nearly constant at all energies and that the diameter of the electron beam is smaller than that of the laser beam. This ensures that the laser-beam–electron-beam interaction volume remains constant and that the same portion of the metastable atoms created by the electron beam are excited by the laser. When the electron beam expands beyond the laser beam volume, we observe what appears to be an artificial decrease in the cross section. Typically, the electron beam diameter (FWHM) is 2 mm and the laser beam diameter is 5 mm. The $2p$ lifetimes are sufficiently short that the spatial distribution of the $2p$-$1s$ emission intensity is representative of the electron beam current density. Thus we place a narrow (0.4 mm) horizontal slit in front of the monochromator entrance slit (which is vertical) and scan the horizontal slit vertically across the electron beam image so as to determine the size of the electron beam and ensure that the electron beam is entirely within the laser beam diameter. Under these conditions our results are reproducible with a random error of less than 10%.

2. *Apparent and direct metastable cross sections*

As explained earlier, above 90 eV the metastable apparent cross section and the cascade cross section show the same energy dependence, and this provides an absolute calibration of the relative apparent metastable cross section. We use a least-squares method to fit the unscaled energy dependence of the apparent metastable cross section obtained from the LIF signal $S_1 - S_2$ to the absolutely measured cascade cross-section excitation function (described in Sec. IV A) for all energies above 100 eV. The range of acceptable fits is ±10% for the $1s_5$ apparent cross section and ±5% for the $1s_3$. Figures 9 and 10 show the absolute apparent cross sections for the $1s_3$ and $1s_5$ levels resulting from this calibration method. Close

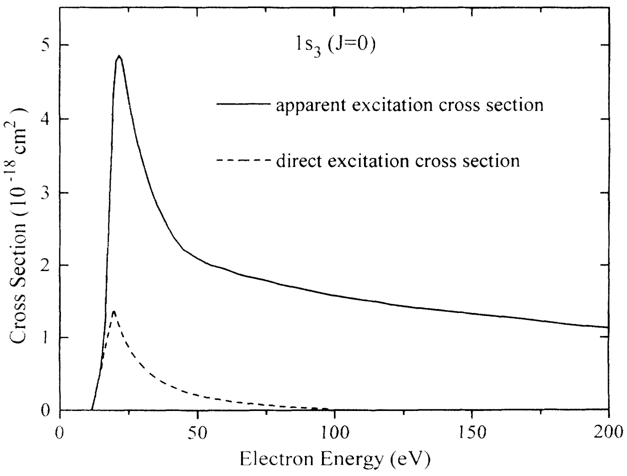

FIG. 9. Plots of the absolute apparent and direct excitation cross section versus electron energy for the $1s_3(J=0)$ metastable level.

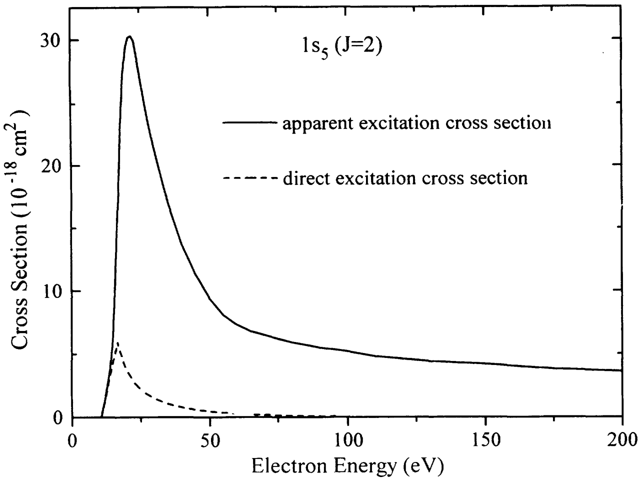

FIG. 10. Plots of the absolute apparent and direct excitation cross section versus electron energy for the $1s_5(J=2)$ metastable level

examination of the excitation functions reveals that a few eV beyond the threshold energy, the excitation function changes slope as one expects when the direct excitation of the metastable level is supplemented by the cascade contribution. We estimate the total uncertainty in the apparent excitation functions to be 25% for the $1s_5$ and 20% for the $1s_3$. These estimates are based on the uncertainties in the absolute cascade cross-section measurements, the statistical error in the unscaled LIF measurement, and the fitting of the metastable apparent excitation function to the cascade excitation function for electron energies above 100 eV.

The direct cross section is the difference between the apparent and cascade curves, as Eq. (3) indicates. Because the cascade cross section is a significant portion of the metastable apparent cross section, the difference between the two curves is small, especially in the tail of the excitation function. There is consequently a fair amount of scatter in this difference. The direct cross sections for electron energies beyond the peak are determined by fitting a smooth curve to all data points at these energies. Figures 9 and 10 also show the $1s_3$ and $1s_5$ direct cross sections. The estimated uncertainties in the maximum values are ±30% and ±25% for the $1s_5$ and $1s_3$ levels, respectively.

We have performed the LIF experiments at different pressures for an electron energy of 22 eV. As indicated in Sec. IV A, the cascade cross sections used for absolute calibration must be measured at each pressure chosen for the LIF experiment. Moreover, care must be taken to maintain a consistent, repeatable interaction volume because for a given setting of the electron-gun grid voltages, the electron beam diameter may change significantly for different pressures. The apparent cross sections obtained from these experiments are somewhat different at different pressures because of the pressure dependence of the cascade cross section discussed earlier (Sec. IV A). However, upon subtracting the cascade from the apparent cross section, we find no difference, within experimental uncertainty, in the direct cross section for the $1s_3$ level obtained from measurements at 3 mTorr and at 6 mTorr. Likewise, we have determined the $1s_5$ direct cross section from data taken at 3 and 11 mTorr, and no discernable difference is found in the results. Within our experimental uncertainties for this procedure (30%), we find no pressure dependence in the direct cross sections for the metastable levels.

We have also verified that S_{LIF} varies linearly with electron beam current. Paying attention to electron beam diameter, we measure the metastable apparent cross section at several energies between 20 and 50 eV and find that it is independent of beam current in our operating regime of 100 to 500 μA. By extension, since the cascade cross sections are also found to be independent of beam current, then the direct metastable cross sections must also be independent of the beam current.

The shape of the excitation function for the $1s_5$ level of Ar is independent of the b and c levels we choose. We observe no distinguishable change in the energy dependence derived from observations of $1s_5 \rightarrow 2p_2 \rightarrow 1s_2$, $1s_5 \rightarrow 2p_2 \rightarrow 1s_3$, or $1s_5 \rightarrow 2p_7 \rightarrow 1s_4$ as our $a \rightarrow b \rightarrow c$ path. This supports the validity of the approximation $A_a \ll A_b$ in our derivation of the proportionality between S_{LIF} and $Q^{\text{app}}(a)$. There are also multiple $a \rightarrow b \rightarrow c$ paths available originating from the $1s_3$ level, but we are unable to perform this test on the $1s_3$ level because all but one of the $1s_3 \rightarrow 2p_i$ transitions are in the infrared, beyond the range of our dye laser. This independence of the results from the $a \rightarrow b \rightarrow c$ path was also found in the cw experiments of Ref. [7].

3. *Number density*

In Eq. (25) we derived an expression to calculate the metastable number density within a small volume ΔV at the center of the electron beam. To apply this expression, we measure the LIF and steady-state signals S'_{LIF} and S_2, and their respective polarizations, as well as the ground-state density n and the total electron beam current I present when measuring S_2. In addition, we use the geometric quantities ΔV and the monochromator slit width w. Equation (25) also requires the transition rate A_{bc} and the other transition rates that contribute to r_2 [14]. Determination of the absolute number density requires $Q^{\text{opt}}(b,c)$ which we measure using the apparatus described in Sec. III B.

In the derivation of Eq. (25) we assumed that the metastable density $n^{\text{init}}(a)$ is constant over ΔV, which in the present experiment is a right circular cylinder 0.4 mm in height and 0.8 mm in diameter located at the center of the electron beam (see Fig. 4). Careful measurement of the steady-state intensity emitted from different horizontal slices of the electron beam indicates that the beam current density and thus $n^{\text{init}}(a)$ vary by only a few percent within the volume ΔV.

We find that the ratio of the number density of $1s_5$ metastable atoms to ground-state atoms in the electron beam at 22 eV is on the order of 10^{-5}. At 5.6 mTorr of Ar and with an electron beam of 22 eV, 300 μA, and diameter 2.3 mm (FWHM), we measured the $1s_5$ density to be 1.8×10^9 atoms cm^{-3} within the volume ΔV. We also observe that under identical experimental conditions the $1s_3$ number density is smaller than the $1s_5$ number density by a factor of 5.1 ± 1.5. This is consistent with the ratio of 6.1 ± 2.0 in the apparent cross sections at this energy.

As explained in Sec. II C 3, when we use Eq. (25) to measure the $1s_5$ density there is a factor of $\frac{5}{3}$ or $\frac{5}{4}$ introduced to account for the unpumped Zeeman states when we use the $J_a=2\rightarrow J_b=1$ or the $J_a=2\rightarrow J_b=2$ path, respectively. Our measurements of the $1s_5$ density by these two different paths agree within our experimental uncertainty.

4. *Polarization*

When we pump the $1s_3(J=0)$ metastable level to the $2p_2(J=1)$ level, the fluorescence into the $1s_2(J=1)$ level (the decay channel with the largest branching ratio) should be nearly completely polarized along the axes perpendicular to the laser polarization. This happens because the metastable atoms are only pumped into the $m_J=0$ state of the $2p_2(J=1)$ manifold if we take the axis of quantization to coincide with the laser's linear polarization. There cannot be any radiation polarized in the $\hat{\mathbf{k}}$ direction because the matrix element

$$\langle cJ_c=1,\, m_J=0|\hat{\mathbf{k}}\cdot\mathbf{r}|bJ_b=1,\, m_J=0\rangle=0\ .$$

The transition matrix element is nonzero only for fluorescence polarized in the $\hat{\mathbf{i}}$ and $\hat{\mathbf{j}}$ directions. Nearly 100% polarization for this case was measured for Ne [10]. For Ar we find the polarization to be less than 30%. The small $1s_3$ cross section, the low laser repetition rate, and the attenuation of the polarizer yield a weak signal so that our uncertainty is very large. Dealignment of the $2p$ level by collisions with Ar atoms may cause a reduction of the observed polarization. The cross section for the collisional dealignment of the $2p_2$ level given by Grandin and Husson [15] is in the neighborhood of 10^{-14} cm^2. Under our experimental conditions this results in a dealignment rate of roughly 10^4 s^{-1}. This is much smaller than the spontaneous decay rate of 34×10^6 s^{-1} [14] and so seems by itself insufficient to explain the lack of polarization. Likewise, the dealignment rate due to electron-atom collisions is also much smaller than the spontaneous decay rate. At this point we have no explanation for the lack of observed polarization.

In order to measure the $1s_5(J=2)$ density, if we pump into the $2p_7(J=1)$ level with the laser, then the resulting fluorescence into the $1s_4(J=1)$ level is isotropic, provided that the $1s_5(m_J=0,\pm1)$ states are equally populated by the electron beam excitation. Although Percival and Seaton [16] have indicated that at threshold energies only the $m_J=0$ state of the excited level is populated by electron excitation, at higher energies the Zeeman states are more equally populated, especially when cascade is significant. In Ref. [10] it is shown that in the case of Ne at 18.2 eV (1.6 eV above threshold), the populations of the individual Zeeman states are virtually identical. Our analysis of Ar indicates a polarization of less than 10%, though the low repetition rate of the YAG laser reduces our sensitivity relative to Ref. [10].

5. *Disappearance rates*

To study the metastable disappearance rates, we turn off the steady-state electron beam and trigger the laser a short time later in order to measure the metastable number density. By varying the delay interval between the electron beam cutoff and the laser pulse over the range of 0 to 150 μs, we map the decrease in the metastable atoms after turning off the electron beam excitation. The semilog plot of the results in Fig. 11 shows two linear segments corresponding to exponential decay rates of 97×10^3 s^{-1} and 31×10^3 s^{-1} with weightings of 0.6 and 0.4, respectively. The electron beam cutoff time presently prevents us from detecting modes that decay faster than 250×10^3 s^{-1} so the faster rate we detect may contain a number of higher (faster) modes. A calculation of typical rates for Ar atoms ballistically exiting the interaction volume at thermal velocities is in general agreement with the faster decay rate, but cannot explain the presence of the slower value. To understand this behavior, we note that the mean free path is given by $\lambda=(\sqrt{2}\pi n\xi^2)^{-1}$ [17], where n is the ground-state density and ξ is the average of the ground-state and metastable diameters. The radius of the ground-state Ar atoms has been given as 1.85×10^{-8} cm [17]. The atomic radius used here can be considered as an effective distance from the nucleus where the electron density decreases to a certain "small fraction" of its peak value, so that beyond this distance the electron charge distribution contributes insignificantly to the interatomic collision cross sections. However, we do not have an *a priori* theoretical criterion to predict this "small fraction." Nevertheless, by examining the electron charge distribution of the metastable and ground-state atoms, we can ascertain the ratio of the radius of the metastable atom to the radius of the ground-state atom in the following way: using the

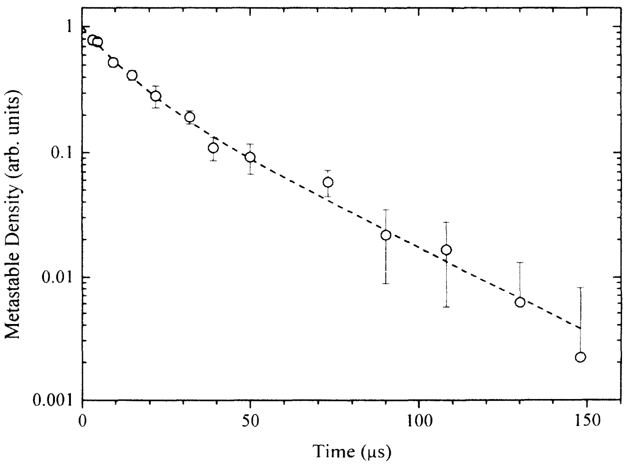

FIG. 11. Plot of the relative metastable number density versus time after the electron beam cutoff. The solid curve is a least-squares fit to the data of the function $a_1\exp(-\gamma_1 t)+a_2\exp(-\gamma_2 t)$, where $a_1=0.4$, $\gamma_1=31\times10^3$ s^{-1}, $a_2=0.6$, and $\gamma_2=97\times10^3$ s^{-1}.

Hartree-Fock $3p$ wave function of the ground state [18], we determine the radial distances r_k at which the electron charge density is k times smaller than its maximum value with k up to 40. This calculation is repeated for the $4s$ Hartree-Fock wave function [19] for the $3p^5 4s$ configuration, yielding the corresponding radial distance r_k' for the metastable atom. We examine the ratio r_k'/r_k and find it remarkably constant, within the range 3.4 to 3.0 for $k=2$ to 40. Thus we take the ratio of the radius of the metastable Ar atom to that of the ground-state atom as 3.2. Using our data-collection pressure 3 mTorr, this gives a mean free path of 0.38 cm. From an experiment on electron emission from the cathode in a Townsend discharge, Molnar deduced the ratio of the metastable radius to the ground-state radius as 2.52 [20]. This corresponds to a mean free path of 0.55 cm at 3 mTorr. Both paths lengths are smaller than the radius of the Faraday cup in which the metastable production occurs, suggesting that a diffusive model is appropriate for analyzing the disappearance of the metastable atoms.

We first compare our experimentally obtained slower decay rate with that predicted by diffusion theory. The general solution for the time dependence of the diffusion equation contains many exponential decay modes and is consistent with our observation of a multimode decay. As a starting point, we choose a cylindrical geometry to analyze the experimental arrangement. The complete, time-dependent solution for the density N of metastable atoms diffusing in a cylinder of radius r_0 and length L is [21]

$$N(r,z,t)=\sum_{m,n=1} G_{mn} J_0(\alpha_m r)\cos[(2n-1)\pi z/L] \times\exp[-\Gamma_{mn} t] , \tag{27}$$

and the decay rates for the modes, characterized by the indices m and n, are

$$\Gamma_{mn}=D\left[\alpha_m^2+\left[\frac{(2n-1)\pi}{L}\right]^2\right] , \tag{28}$$

where D is the diffusion constant, $\alpha_m r_0$ is the mth root of the zeroth-order Bessel function of the first kind, and the G_{mn} are the weightings of the modes. The m index indicates the radial mode number and the n index identifies the longitudinal mode.

To estimate the theoretical decay rate from Eq. (28), we use $D=\lambda v/3$ [17], where $\lambda=0.38$ cm as calculated previously and an average thermal velocity of the Ar atoms of $v=3.9\times10^4$ cm s^{-1}. The physical dimensions of the Faraday cup in which the diffusion occurs are $r_0=0.9$ cm and $L=10$ cm. Substituting these values into Eq. (28), we find that according to diffusion theory, $\Gamma_{11}=37\times10^3$ s^{-1}, which is quite close to our experimental value. If we use $\lambda=0.55$ cm, Γ_{11} becomes 53×10^3 s^{-1}, still in reasonable agreement with our experiment in view of the approximations involved. The cylindrical symmetry of our collision region is distorted by the presence of the viewing slits on the sides of the Faraday cup and apertures above and below the collision region (to admit the laser beam). This may explain why the calculated values of Γ_{11} are too large since the metastable atoms that escape through these openings are free to diffuse to the walls of the vacuum chamber 5 cm away, thus increasing the effective diameter of the cylindrical enclosure. Such an increase in the diameter would result in a decrease in the calculated Γ_{11}.

We next compare the relative weighting of our experimental slow decay rate with that predicted by diffusion theory. To do this, we obtain the steady-state (initial) metastable spatial distribution from the solution of the time-independent, steady-state diffusion equation and then match Eq. (27) to this solution to determine the weightings G_{mn} of the modes. The translational symmetry in the z direction (along the electron beam) suggests that higher longitudinal modes are unlikely to contribute. If one assumes that the metastable density is roughly uniform along the z axis, except at the ends where it is zero, it is clear that in expanding this distribution with cosines according to Eq. (27), the fundamental ($n=1$) term dominates. We then turn our attention to the radial portion of the steady-state diffusion equation [22]:

$$-D\left[\frac{\partial^2 N}{\partial r^2}+\frac{1}{r}\frac{\partial N}{\partial r}\right]=\frac{nj(r)}{e}Q^{\mathrm{app}}(\mathrm{met}) , \tag{29}$$

where $Q^{\mathrm{app}}(\mathrm{met})$ refers to the metastable apparent cross sections. If we solve the simple case where the electron beam current density $j(r)$ is constant inside the electron beam of radius r_e and zero for $r>r_e$, then the solutions for the metastable density are

$$N(r)=\begin{cases}\dfrac{k}{4}\left\{r_e^2\left[1+2\ln\left[\dfrac{r_0}{r_e}\right]\right]-r^2\right\}, & 0\le r\le r_e\\[2ex] \dfrac{k}{2}r_e^2\ln\left[\dfrac{r_0}{r}\right], & r_e\le r\le r_0\end{cases} \tag{30}$$

where

$$k=[nIQ^{\mathrm{app}}(\mathrm{met})]/[De\pi r_e^2]$$

and I is the total electron beam current. We match the radial part of Eq. (27) to this solution in order to determine the weightings of the radial modes. For a typical electron beam radius of 0.14 cm and a Faraday cup radius of 0.9 cm, the normalized weight of the fundamental ($m=n=1$) mode relative to all others is approximately 0.5, in qualitative agreement with our experimental finding of 0.4. If we allow for slightly larger effective Faraday cup radius as discussed in the preceding paragraph, the weight of the fundamental mode decreases slightly and comes even closer to the experimental value.

We also solve for the initial metastable distribution using a more realistic beam current density distribution. From observation we have verified that the electron beam current density distribution is well described by a Gaussian function. The solution for $N(r)$ is obtained numerically and the result is very similar to Eq. (30): the values for $N(r)$ obtained for the Gaussian current distribution are within 10% of the values in Eq. (30) for all r. The weightings of the modes are therefore also very similar.

To complete this discussion, we consider the fast decay modes. If we neglect the higher longitudinal modes as explained earlier, the next higher rate as determined from Eq. (28) is Γ_{21}, which is found to be five times larger than Γ_{11}. Although this ratio is larger than we found experimentally, it is qualitatively similar. The quantitative discrepancy may again be the result of the approximation of a cylindrical geometry.

The results of this preliminary investigation of the metastable disappearance rates are in qualitative agreement with diffusion theory. Further studies involving a variety of pressures and Faraday cup geometries would provide valuable points for a more comprehensive analysis.

C. Other work

1. *Experiment*

Other researchers have previously employed several alternate experimental methods to investigate the Ar metastable cross sections. Early studies were measurements by Lloyd *et al.* [23] and Borst [24] using the time-of-flight (TOF) technique. The TOF technique uses a highly monochromatic electron beam pulse incident on a beam of ground level Ar atoms, and the excited atoms move toward a detector a few centimeters away. The collision with the detector surface produces secondary electrons, which are amplified by an electron multiplier. The distance between the metastable source and the detector is sufficiently large that all nonmetastable Ar species decay before reaching the detector and the photons emitted from excited Ar levels arrive long before the fastest metastable atoms. By varying the energy of the electrons in the pulse and monitoring the electron beam current, the energy dependence of the sum of the $1s_3$ and $1s_5$ apparent metastable cross sections can be ascertained.

Borst reports on absolute value for the sum of the apparent cross sections,

$$Q^{\text{app}}(1s_3)+Q^{\text{app}}(1s_5)\ ,$$

based on his calibration of the secondary electron yields of his metastable detector. The maximum cross section of 3.5×10^{-17} cm^2 reported by Borst is the same as our maximum value. The other TOF measurements are relative excitation functions: Mason and Newell [25] duplicated Borst's excitation function shape up to 50 eV and extended the energy range from 50 to 142 eV. Theuws, Beijerinck, and Verster [26] also reported the relative values of

$$Q^{\text{app}}(1s_3)+Q^{\text{app}}(1s_5)$$

and obtained an energy dependence in general agreement with Ref. [24]. All of the TOF excitation functions are similar in shape, with a narrow peak at 22 eV and falling away rapidly at higher energies.

Figure 12 shows our results for the sum of the metastable apparent cross sections ($1s_3+1s_5$) plotted with the TOF measurements of other workers. All curves have been normalized to the same peak value. The agreement at lower electron energies is very good but at energies greater than 100 eV our cross section is approximately twice as large as the other measurements. At these energies the apparent cross section is essentially composed of only cascade cross section. We believe this discrepancy is due to the earlier described pressure effects in the cascade cross section that cause the cross sections at high energies to increase relative to the peak cross section as the pressure increases. We have made measurements at pressures of 0.35 mTorr and found that the cascade cross sections between 100 and 200 eV at this low pressure are roughly half their values at 3.0 mTorr; this would bring down the value of our high-energy tail to coincide with the TOF results. The TOF measurements are taken in a system using a beam of ground level atoms against a relatively low background gas pressure. This results in an optically thin path for the emitted radiation to follow to reach the detector, whereas our system employs a static Ar pressure of 3 mTorr and consequently there is more opportunity for radiation trapping. This lends support to our earlier hypothesis that the cascade cross-section pressure effects we observe are caused, at least in part, by radiation trapping.

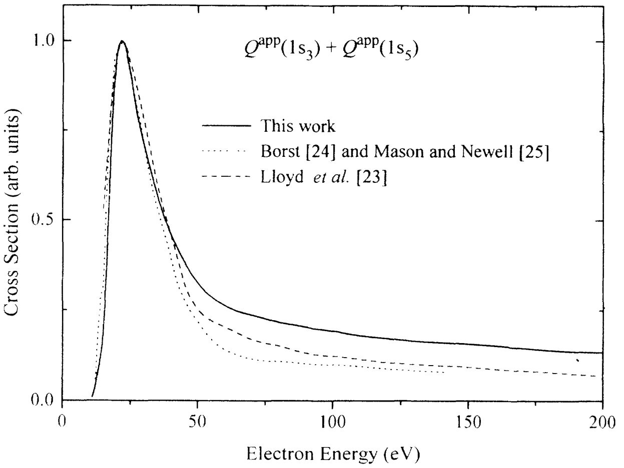

FIG. 12. Comparison of experimental results for the energy dependence of $Q^{\text{app}}(1s_3)+Q^{\text{app}}(1s_5)$. The discrepancy at higher energies can be attributed to radiation trapping (see Sec. IV C 1).

Mityureva and Smirnov [27] recently measured the individual apparent cross sections for the $1s_3$ and $1s_5$ levels using optical absorption out of the metastable level. Their cross sections at the maximum of the excitation functions are 34×10^{-18} cm^2 for the $1s_5$ level and 9.0×10^{-18} cm^2 for the $1s_3$ level at 18 eV. Both of these values are approximately 4×10^{-18} cm^2 larger than our peak values and occur at a lower energy.

Chutjian and Cartwright [28] measured the differential cross sections for the individual $1s_3$ and $1s_5$ levels using electron-energy-loss spectroscopy. By extrapolating the differential cross sections to unmeasured angles and integrating over all scattering angles, they obtain the total (integral) cross section for direct excitation into the $1s_3$ and $1s_5$ levels. Figure 13 contains plots of their direct excitation data for the $1s_3$ level along with ours. Their $1s_3$ data are within quoted experimental uncertainties of our values for all energies except 20 eV, where their result is much smaller than ours. Figure 14 compares the $1s_5$

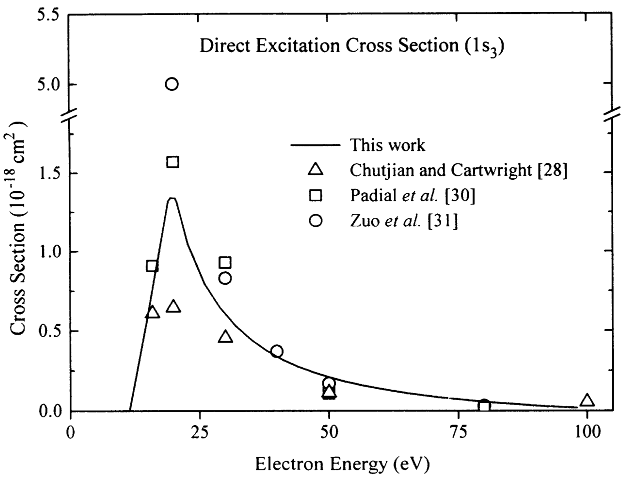

FIG. 13. Comparison of experimental and theoretical results for the energy dependence and magnitude of the direct excitation cross section for the $1s_3(J=0)$ metastable level.

data. For the $1s_5$ level the agreement between their data and ours is very good for all energies except 17 eV and even this data point falls within the experimental uncertainty of our data. In addition, our work and that of Ref. [28] indicate that the peak cross section of the $1s_5$ level occurs at a slightly lower energy than that of the $1s_3$ level.

2. *Theory*

We have found in the literature theoretical calculations for the direct electron excitation cross sections of the $1s_3$ and $1s_5$ levels of Ar reported by three groups. Sawada, Purcell, and Green [29] used a distorted-wave formulation with exchange to calculate the direct excitation cross section for the composite triplet component of the $1s$ manifold. In reference to our analysis, this composite includes not only the $1s_3$ and $1s_5$ levels but also the "triplet portions" of the $1s_2$ and $1s_4$ resonance levels. It is thus difficult to compare it to our data, which consist of only the two metastable levels.

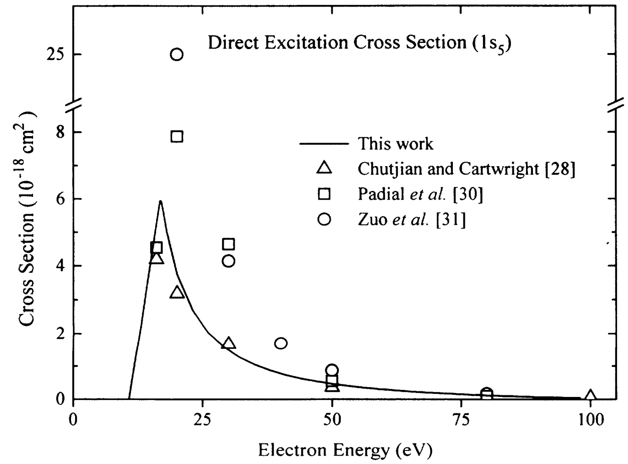

FIG. 14. Comparison of experimental and theoretical results for the energy dependence and magnitude of the direct excitation cross section for the $1s_5(J=2)$ metastable level.

Padial *et al.* [30] used first-order, many-body theory (FOMBT) to calculate the differential and total (integral) cross sections for each of the metastable levels for energies from 16 to 80.4 eV. Their cross sections for the $1s_3$ level agree reasonably well with our results and the $1s_5$ level cross sections are somewhat larger than ours. Zou, McEachran, and Stauffer [31] have also calculated differential cross sections for electron-impact excitation of the $1s_3$ and $1s_5$ levels of Ar. The integrated cross sections obtained from their differential cross-section data at 20 eV are 5.0×10^{-18} and 25×10^{-18} cm^2 for the $1s_3$ and $1s_5$ levels, respectively, which are larger than our results. At higher energies the results of Ref. [31] are similar to those of Ref. [30]. Figures 13 and 14 show the data of Refs. [28], [30], and [31] for the $1s_3$ and $1s_5$ levels, respectively, plotted with ours.

If we assume that the direct cross section for the $1s_3(J=0,m=0)$ state is the same as each of the $1s_5(J=2)$ states, then the ratio of the total direct cross sections for the two levels should be approximately the same as the ratio of their statistical weights; for $1s_5$ versus $1s_3$ this is 5 to 1. The FOMBT calculations of Refs. [30] and [31] agree with this ratio, but Khakoo *et al.* [32] performed an experiment that explicitly measured this ratio at 30 eV and found the ratio of the differential cross sections to be less than 4.4 for all angles measured. Our results give a ratio for the total direct cross sections at 30 eV of about 3.0 ± 1.1 and a ratio for the direct peak cross sections of about 4.3 ± 1.5. In Ref. [32] Khakoo *et al.* also reported similar measurements for Ne where the ratio is close to 5 for scattering angles of 30° or greater, but decreases considerably for smaller scattering angles. More recently, Khakoo *et al.* [33] have presented new results for Ne and their new ratio is close to 5 for the entire range of the scattering angles measured. The ratio of the (integrated) direct cross sections for the $1s_5$ and $1s_3$ levels of Ne determined by the LIF technique [7] is generally close to 5, being 5.5, 5.2, 4.9, 4.4, and 3.7 at 25, 30, 35, 40, and 50 eV, respectively.

V. CONCLUDING REMARKS

We use the technique of laser-induced fluorescence in conjunction with a high-power, pulsed laser to measure the electron excitation cross sections for the $1s_5$ and $1s_3$ metastable levels of argon. A monoenergetic electron beam excites the ground-state atoms into the metastable level, and a pulsed dye laser pumps the metastable atoms to a higher level. As this higher level spontaneously decays, we observe the emission. We show that the transient laser-induced fluorescence is directly proportional to the apparent cross section of the metastable level and to the metastable number density. We perform auxiliary experiments to measure the absolute optical emission cross sections for the cascade transitions into the metastable levels. We use these cascade cross sections to put the relative apparent excitation function on an absolute scale by taking advantage of the fact that the direct cross section for a purely triplet metastable level diminishes very rapidly with increasing incident electron energy so that at high incident electron energies (above 90 eV) the apparent cross section of the metastable level is essentially equal to the cascade cross section. The maxima of the apparent cross sections are 4.9×10^{-18} and 30×10^{-18} cm^2 for the $1s_3$ and $1s_5$ levels, respectively. By subtracting the cascade cross section from the apparent cross section, we determined the direct metastable cross sections. The maximum direct cross section for the $1s_3$ level is 1.4×10^{-18} cm^2 and for the $1s_5$ level it is 6.0×10^{-18} cm^2.

We also show the applicability of the pulsed laser system for measuring absolute metastable number densities. At the center of the electron beam, the ratio of metastable to ground level atoms is on the order of 10^{-5}. This technique also allows us to measure the disappearance rates for the metastable atoms. We turn off the electron beam before the laser pulse arrives in the interaction volume and, by varying the interval between the electron beam cutoff and the laser beam arrival, we determine the relative metastable population versus time after the electron beam cutoff. We observe two decays modes that are qualitatively explicable by diffusion theory.

The pressure effects we observed in the $2p$-$1s$ family of optical cross sections deserve further investigation for intrinsic reasons although they do not influence our results for the direct excitation cross sections of the metastable levels. Radiation trapping of levels above the $2p$ levels is at least partly responsible for these effects. The population distribution among the $1s_5$ states and the related possible depolarization effects in the $2p$ levels also merit additional study in the future.

ACKNOWLEDGMENTS

We thank Dr. S. Chung for providing us with the Hartree-Fock wave functions for the metastable Ar atom. This research work is supported by the U.S. Air Force Office of Scientific Research and the National Science Foundation, Grant No. PHY-9005895.

APPENDIX

The optical Bloch equations are a useful tool with which to analyze coherent, closed, two-level systems. The formalism was originally developed to analyze spin-$\frac{1}{2}$ systems and so it is based on a closed, two-level system. By the suitable choice of the quantization axis, most laser-pumped atomic systems can fulfill this requirement quite well. The optical analog to the Bloch equations are

$$\frac{du}{dt}=-\delta v-u\Gamma_2\ , \tag{A1}$$

$$\frac{dv}{dt}=-\delta u-v\Gamma_2+\Omega w\ , \tag{A2}$$

$$\frac{dw}{dt}=-(w-w_0)\Gamma_1-\Omega v\ , \tag{A3}$$

where u and v are the components of the atomic dipole moment in phase and in quadrature with the laser field, respectively. The actual level populations are contained in the inversion term

$$w=\frac{n(b)-n(a)}{n(b)+n(a)}\ . \tag{A4}$$

The prelaser value of w is $w_0=-1$. The upper level spontaneous decay rate is Γ_1 and the coherence relaxation rate is Γ_2. Any process that disturbs the dipole oscillation of the resonant atom contributes to this relaxation rate. Such processes include spontaneous emission, collisions (with atoms and electrons), and the effect of inhomogeneous Doppler broadening. The detuning of the laser from resonance is δ and the Rabi frequency Ω is proportional to the laser intensity.

The solutions to the Bloch equations all have the form [34]

$$X(t)=Ae^{-at}+\left[B\cos(st)+\frac{C}{s}\sin(st)\right]e^{-bt}+D\ , \tag{A5}$$

where X represents u, v, or w. For the solution of w, $a=\Gamma_2$, $b=(\Gamma_1+\Gamma_2)/2$, and the steady-state coefficient D is

$$D=w_0\frac{1+(\delta\Gamma_2)^2}{1+(\delta\Gamma_2)^2+\Gamma_1\Gamma_2\Omega^2}\ . \tag{A6}$$

The rate at which w approaches D is governed by Γ_2. If Γ_2 is large, the Rabi oscillations of the populations (and the coherences) induced by the laser dampen out rapidly and w quickly reaches its steady-state equilibrium value D. In conditions like this, where the coherences are negligible, ordinary rate equations are a special case of the coherent Bloch equation for the inversion [Eq. (A3)] and can be used to determine the level populations. For small laser detuning δ and large laser powers (large Ω), D becomes nearly zero. This means that the upper and lower level populations are equal when the atomic system is in equilibrium with the laser field.

Several aspects of our laser system allow us to use rate equations. For a broadband laser like ours, more than one mode may excite the transition. The absence of any phase relationship between the modes in our free-running laser prevents optical coherences from developing [35]. Even in the event of only one mode at a time exciting the transition, the power in the mode will vary from shot to shot. When the laser power in a pulse changes, the frequency of the inversion oscillation changes. Over many shots the average of the inversion will tend toward its steady-state value of zero. Furthermore, the Doppler distribution is broad enough that Γ_2 will be shorter than the laser pulse duration and so the Rabi oscillations will be well damped out before any measurements are taken.

[1] J. T. Dakin, IEEE Trans. Plasma Sci. **19**, 991 (1991).

[2] See, for example, C. Brau, in *Excimer Lasers,* edited by C. K. Rhodes (Springer, Berlin, 1979); G. J. Fetzer, J. J. Rocca, G. J. Collins, and R. Jacobs, J. Appl. Phys. **60**, 2739 (1986).

[3] R. S. Van Dyck, Jr., C. E. Johnson, and H. A. Shugart, Phys. Rev. A **5**, 991 (1972).

[4] A. I. Korotkov and N. A. Khromov, Opt. Spektrosk. **69**, 1219 (1990) [Opt. Spectrosc. (USSR) **69**, 721 (1990)].

[5] F. A. Sharpton, R. M. St. John, C. C. Lin, and F. E. Fajen, Phys. Rev. A **2**, 1305 (1970).

[6] J. K. Ballou, C. C. Lin, and F. E. Fajen, Phys. Rev. A **8**, 1797 (1973).

[7] M. H. Phillips, L. W. Anderson, and C. C. Lin, Phys. Rev. A **32**, 2117 (1985).

[8] T. R. O'Brian and J. E. Lawler, Phys. Rev. A **44**, 7134 (1991).

[9] C. C. Lin and L. W. Anderson, Adv. At. Mol. Opt. Phys. **29**, 1 (1992).

[10] J. O. Phelps, M. H. Phillips, L. W. Anderson, and C. C. Lin, J. Phys. B **16**, 3825 (1983).

[11] H. L. Zhang, D. H. Sampson, and Robert E. H. Clark, Phys. Rev. A **41**, 198 (1990).

[12] A. R. Filippelli, S. Chung, and C. C. Lin, Phys. Rev. A **29**, 1709 (1984).

[13] M. S. Feld, M. M. Burns, T. U. Kühl, P. G. Pappas, and D. E. Murnick, Opt. Lett. **5**, 79 (1980).

[14] W. L. Wiese, J. W. Brault, K. Danzmann, V. Helbig, and M. Kock, Phys. Rev. A **39**, 2461 (1989).

[15] J. P. Grandin and X. Husson, J. Phys. (Paris) **39**, 933 (1978).

[16] I. C. Percival and M. J. Seaton, Philos. Trans. R. Soc. London, Ser. A **251**, 113 (1958).

[17] A. V. Roth, *Vacuum Technology* (North-Holland, New York, 1976).

[18] E. Clementi and C. Roetti, At. Data Nucl. Data Tables **14**, 177 (1974).

[19] S. Chung (private communication).

[20] J. P. Molnar, Phys. Rev. **83**, 940 (1951).

[21] E. W. McDaniel and E. A. Mason, *The Mobility and Diffusion of Ions in Gases* (Wiley, New York, 1973).

[22] F. Chen, *Introduction to Plasma Physics and Controlled Fusion* (Plenum, New York, 1984).

[23] C. R. Lloyd, E. Weigold, P. J. O. Teubner, and S. T. Hood, J. Phys. B **5**, 1712 (1972).

[24] W. L. Borst, Phys. Rev. A **9**, 1195 (1974).

[25] N. J. Mason and W. R. Newell, J. Phys. B **20**, 1357 (1987).

[26] P. G. A. Theuws, H. C. W. Beijerinck, and N. F. Verster, J. Phys. E **15**, 328 (1982).

[27] A. A. Mityureva and V. V. Smirnov, Opt. Spektrosk. **59**, 501 (1985) [Opt. Spectrosc. (USSR) **59**, 303 (1985)].

[28] A. Chutjian and D. C. Cartwright, Phys. Rev. A **23**, 2178 (1981).

[29] T. Sawada, J. E. Purcell, and A. E. S. Green, Phys. Rev. A **4**, 193 (1971).

[30] N. T. Padial, G. D. Meneses, F. J. da Paixão, G. Csanak, and D. C. Cartwright, Phys. Rev. A **23**, 2194 (1981).

[31] T. Zuo, R. P. McEachran, and A. D. Stauffer, J. Phys. B **25**, 3393 (1992).

[32] M. A. Khakoo, T. Tran, D. Bordelon, and G. Csanak, Phys. Rev. A **45**, 219 (1992).

[33] M. A. Khakoo, C. E. Beckman, S. Trajmar, and G. Csanak, *Abstracts of the XVIIIth International Conference on the Physics of Electronic and Atomic Collisions, Aarhus, Denmark, 1993,* edited by T. Andersen, B. Fastrup, F. Folkmann, and H. Knudsen (IFA, Aarhus University, Aarhus, 1993), p. 174.

[34] H. C. Torrey, Phys. Rev. **76**, 1059 (1949).

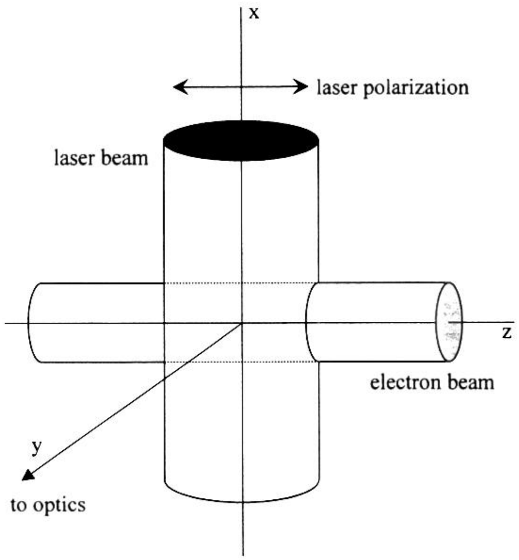

FIG. 4. Geometry of the LIF interaction region for cross-section measurements. The electron beam propagates along the z axis (the quantization axis). The laser beam propagates parallel to the x axis and is linearly polarized along the z axis. The fluorescence is detected along the y axis.

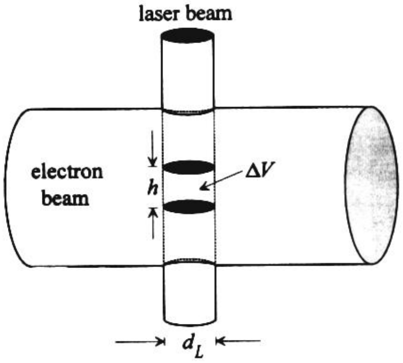

FIG. 5. Geometry of the LIF interaction region for absolute number density measurements. This figure is similar to Fig. 4, except that the laser beam diameter (d_L) is smaller than that of the electron beam. The observed volume is further reduced to a height h by an auxiliary horizontal slit placed at the entrance slit of the monochromator.